

Article

Syn-Tectonic Dolomite U-Pb Geochronology Constraining Intracontinental Deformation: A Case Study from the Gelouang Gold Deposit in the Qinling Orogen, China

Yi-Xue Gao ^{1,2}, Gui-Peng Jiang ^{2,*}, Yi Qu ¹, Rong-Qing Zhang ³, Yan-Wen Tang ⁴, Rui Zhu ² and Si-Jia Yao ¹¹ School of Earth Sciences and Resources, China University of Geosciences, Beijing 100083, China² Zhaojin Mining Industry CO., LTD., Zhaoyuan 265400, China³ State Key Laboratory for Mineral Deposits Research, School of Earth Sciences and Engineering, Nanjing University, Nanjing 210023, China⁴ State Key Laboratory of Ore Deposit Geochemistry, Institute of Geochemistry, Chinese Academy of Sciences, Guiyang 550081, China

* Correspondence: zgzjianggp@163.com; Tel.: +86-010-82322152

Abstract: Determining absolute ages of orogenic faults is critical to understanding the deformation process in the upper crust, but obtaining age remains a problem due to the lack of readily available techniques. Carbonates occur as veins in faults in a range of geological settings, and thus it is a suitable mineral for U-Pb geochronology. Here, we apply the new approach of U-Pb dating on syn-tectonic dolomite veins from the Gelouang gold deposit in the western Qinling Orogen to unravel the absolute timing of the fault formation shedding new light on the regional upper crustal deformation archive. In situ LA-ICP-MS U-Pb dating of dolomite yielding a successful age of 115–112 Ma demonstrates that the dolomite precipitated coeval with tectonic events ascribed to the post-orogenic deformation phase in the Qinling Orogen. This event is possibly correlated with broader intracontinental processes and might be an inevitable response to the extensional deformation of the Qinling Orogen. The presented LA-ICP-MS dolomite U-Pb age successfully represents the age of a specific structure that encompasses the intracontinental process in the Qinling Orogen. Moreover, it demonstrates the utility of the method to decipher a response to complex deformation histories on a regional scale.

Keywords: in situ U-Pb dating; syn-tectonic dolomite; intracontinental deformation; Qinling Orogen



Citation: Gao, Y.-X.; Jiang, G.-P.; Qu, Y.; Zhang, R.-Q.; Tang, Y.-W.; Zhu, R.; Yao, S.-J. Syn-Tectonic Dolomite U-Pb Geochronology Constraining Intracontinental Deformation: A Case Study from the Gelouang Gold Deposit in the Qinling Orogen, China. *Minerals* **2022**, *12*, 1045. <https://doi.org/10.3390/min12081045>

Academic Editors: Kunfeng Qiu and Paul Alexandre

Received: 1 July 2022

Accepted: 15 August 2022

Published: 19 August 2022

Publisher's Note: MDPI stays neutral with regard to jurisdictional claims in published maps and institutional affiliations.



Copyright: © 2022 by the authors. Licensee MDPI, Basel, Switzerland. This article is an open access article distributed under the terms and conditions of the Creative Commons Attribution (CC BY) license (<https://creativecommons.org/licenses/by/4.0/>).

1. Introduction

Faulting and fracturing studies in the upper crust provide pivotal insights for understanding the mechanics of the pressure-dependent deformation process [1,2]. Moreover, faulting developed in the orogenic belt preserves an archive of how deformation controls landscape development, plate boundary interaction and the crustal deformation process. In addition to investigating the geometry, kinematics, and architecture characteristics, the timing of faults and how faults develop further through time is a prerequisite to establishing the framework of the tectonic evolution [3]. However, the absolute timing of fault slip and fracture formation remains a poorly constrained parameter, possibly due to the absence of syn-kinematic and authigenic minerals and readily available techniques. In general, carbonate is a common fault-hosted mineral that is suitable for U-Pb geochronology and is not fraught with closure temperature issues [4–8]. Recent in situ LA-ICP-MS U-Pb dating of accessory minerals, such as carbonate and monazite, has led to a proliferation of studies in constraining the period of fault [5,9–14], diagenetic event [15–18], fluid flow [19–21], sedimentation [22,23], and mineralization of ore deposits [24–32] as well as magmatic-hydrothermal processes [33–35], demonstrating that this novel method is a powerful technique for determining the absolute timing of deformation in the upper crust.

The Qinling Orogen, which connects the Dabie Orogen to the east and the Qilian and Kunlun Orogens to the west, was formed by subduction and collision between the North

and South China Blocks from the north to the south along the Early Paleozoic Shangdan and Animaqing-Mianlue suture [36,37]. It has been well documented that the whole range involved an intracontinental tectonic process through geological, geophysical, and geochronological investigations on the Mesozoic magmatic and metallogenic events [38–40]. This polyphase deformation was exhibited by sets of fault structures, echelon Cretaceous sedimentary basins and folds that crosscut each other, providing a relative time sequence of the deformation events. Much research up to now has outlined a rough timescale of stages by investigation of magmatism, tectonics events, and indirect thermochronological studies, including U-Pb on zircon, Ar-Ar on hornblende, biotite and K-feldspar, apatite fission-track (AFT), and apatite (U-Th-Sm)/He [41–44]. In contrast, the direct and absolute dating of specific fault motion resulting from Mesozoic intracontinental deformation is poorly constrained.

In this study, syn-tectonic dolomites were targeted from an extensional fault vein that occurs in the Gelouang gold deposit, which cuts the orebody, recording the fracture information. We performed dolomite U-Pb dating in an attempt to provide absolute age constraints on the deformation attributed to the intracontinental process in Qinling Orogen and to elucidate the tectonic evolution history on a regional scale.

2. Geological Setting

The Qinling Orogen, which extends for nearly 1500 km from east to west, is a composite continental orogenic belt traversing the central part of the Chinese mainland (Figure 1a, [37,45–48]). The orogen is tectonically bounded by Qilian Orogen and North China Block by Lingbao-Lushan-Wuyang Fault to the north and by the Songpan-Ganzi basin and Bikou Terrane marked by the Mianlue-Bashan-Xiangguang Fault to the south (Figure 1b, [40,49–51]). From north to south, the Qinling Orogen is divided into four tectonic units, including the south margin of the North China Block, North Qinling Terrane, South Qinling Terrane, and the northern margin of South China Block by three dominant sutures (the Neoproterozoic Kuangping suture, the early Paleozoic Wushan-Tianshui-Shangdan suture, and the Middle Triassic Maqu-Nanping-Lueyang suture, respectively). This orogen was formed by multiple steps of assembly and subsequent collision between the North China Block and the South China Block during the Paleozoic and Late Jurassic [37]. The Paleozoic orogeny is largely marked by the Shangdan suture, which records the existence of subduction and closure of the Shangdan ocean in the Early Paleozoic to Late Triassic [36]. From Late Paleozoic to Late Triassic, the northward subduction and closure of the Mianlue ocean, following the collision, led to the final formation of the tectonic units [37,52]. After the final amalgamation of the North and South China Blocks in the Triassic, the Qinling Orogen evolved into an intracontinental orogen accompanied by strongly compressional deformation [42,53–55].

The Xiahe-Hezuo area is located in the northwestern part of the Qinling Orogen. Northwest-striking structures were well developed during the Triassic orogeny, as represented by the Xiahe-Hezuo fault and Xinpu-Lishishan anticline. This region hosts outcrops of Late Paleozoic to early Mesozoic greenschist-facies slate and Cretaceous volcanic-sedimentary rocks. The fine-grained foliated slate has been metamorphosed from initial clastic and carbonate rocks (Figure 1c, [40,56]). The Carboniferous to Permian marine clastic and carbonates are exposed to the southeast, which dominates the core and flanks of the Xinpu-Lishishan anticline [57,58]. During the Cretaceous, a series of W-E trending intermontane basins formed within the western and central part of Qinling Orogen [59,60]. Mesozoic dioritic to granitic plutons, as well as mafic dikes and sills, are widely distributed in the Xiahe-Hezuo area, accompanied by ore occurrences [42,61–63].

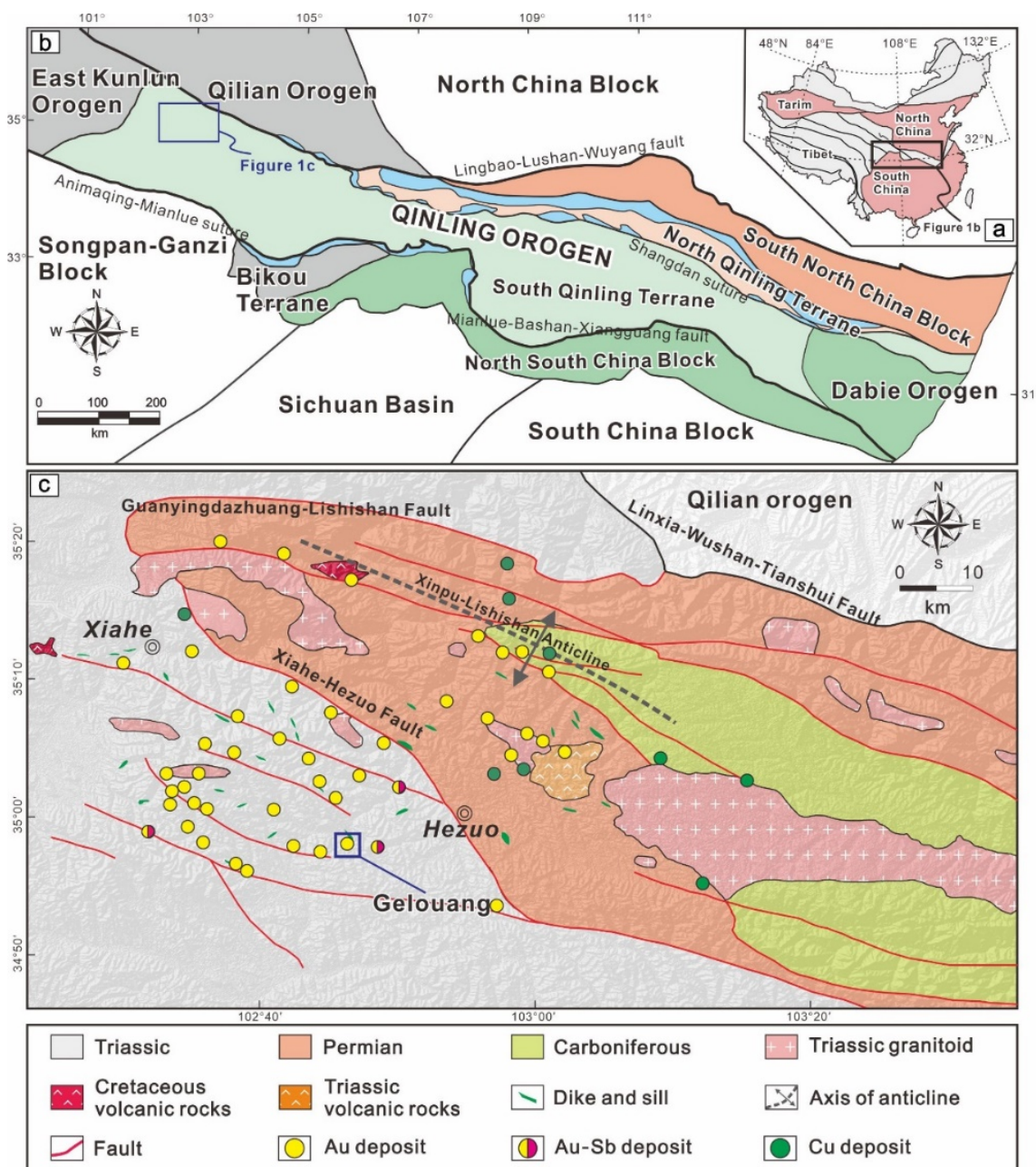


Figure 1. (a,b) Major tectonic domains of China and the location of the Qinling Orogen. (c) Digital elevation model with superimposed geological map of Xiahe-Hezuo district of the western Qinling Orogen showing faulting and ore deposits (modified after [45–47]).

The Gelouang gold deposit is located about 15 km west of Hezuo City in Gansu Province, and with an average grade of 2.18 g/t, approximately 27.7 t Au has been mined to the present day. The deposit is hosted in the metasedimentary rocks of the Triassic Gulangdi Formation and granitic rocks emplaced into the unit. Magmatism at Zaozigou is represented by sills and dikes of intermediate to felsic composition (Figures 1c and 2), which consist of porphyritic dacite, granodiorite, and porphyritic rhyolite (estimate ages of ca. 150 Ma, [64]). Two styles of mineralization have been recognized at Gelouang, which comprise early disseminated and stockwork ores. Ore-related alteration includes sericitization, sulfidation, silicification, and carbonatization of the wall rocks.

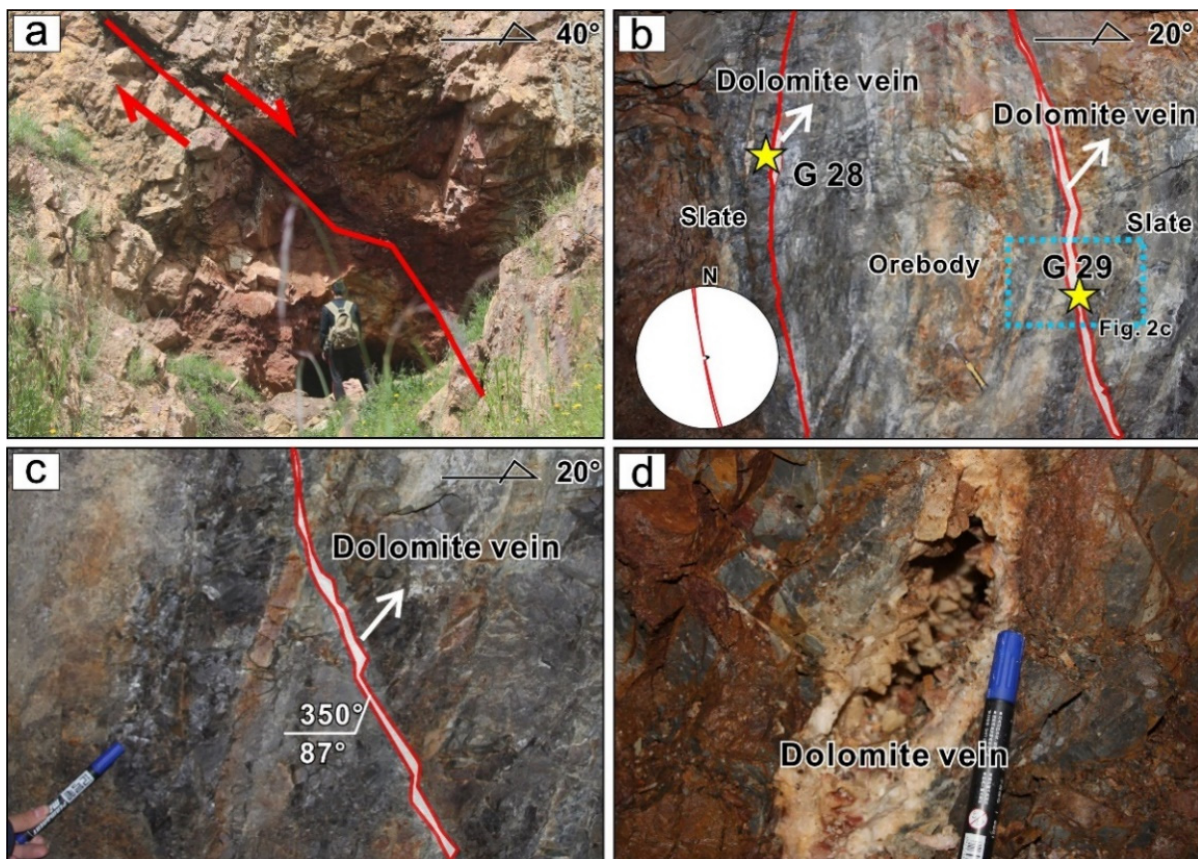


Figure 2. Field photographs to show (a) the fault and associated small-scale features in Gelouang gold deposit. (b) Exposure of the fault from underground works that indicate dolomite veins crosscut the altered slate and orebodies. (c,d) Close-up view on the fault plane.

3. Samples and Methods

3.1. Sampling Description

Dolomite veins were taken from underground workings at the Gelouang gold deposit. The dolomite veins are characterized as syn-tectonic along the N-W trending normal fault and crosscut the orebodies and the wall rock Triassic slate (Figure 2a). We sampled the exposed fresh grey to off-white dolomite veins (G28 and G29, Figure 3), which comprise a single phase with no shear displacement and a swarm of parallel contemporaneous dolomite veinlets in the vicinity. Sample G28 is from dolomite veins, which separate the mineralized slate from quartz veins (Figures 3a and 4), suggesting that the dolomite postdates slate and ore formation. At the center of the sample is a 5 mm thick dolomite vein, where euhedral rhomboid crystals form an elongate vein texture. Sample G29 is light grey with slickenfibres on the fractured fault surface (Figure 3b). Under the microscope, there is a ~200 μm calcite vein related to ore cross-cut by the dolomite vein (Figure 4c). The blocky dolomite crystals are intergrown with the larger dolomite crystals, which, with sizes ranging from 100 μm to 3 mm, are very fine-grained and are all pointed in the same direction as the dolomite veins (Figure 5). The elongated dolomite crystals deformed parallel or oblique to the fracture walls are observed in faults. Dated dolomite crystals are selected from the branches of the dolomite vein.

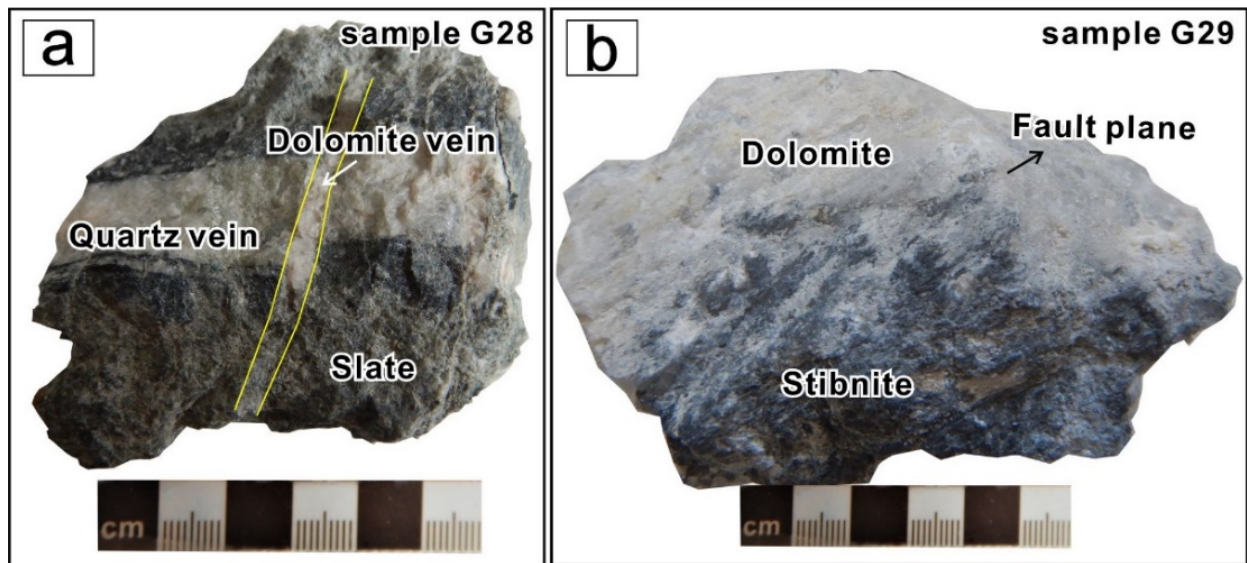


Figure 3. Hand specimen of dolomite veins in samples G28 and G29 from fault plane. (a) dolomite vein from sample G28 separates the mineralized slate from quartz veins. (b) slickenfibres on the fractured fault surface from sample G29.

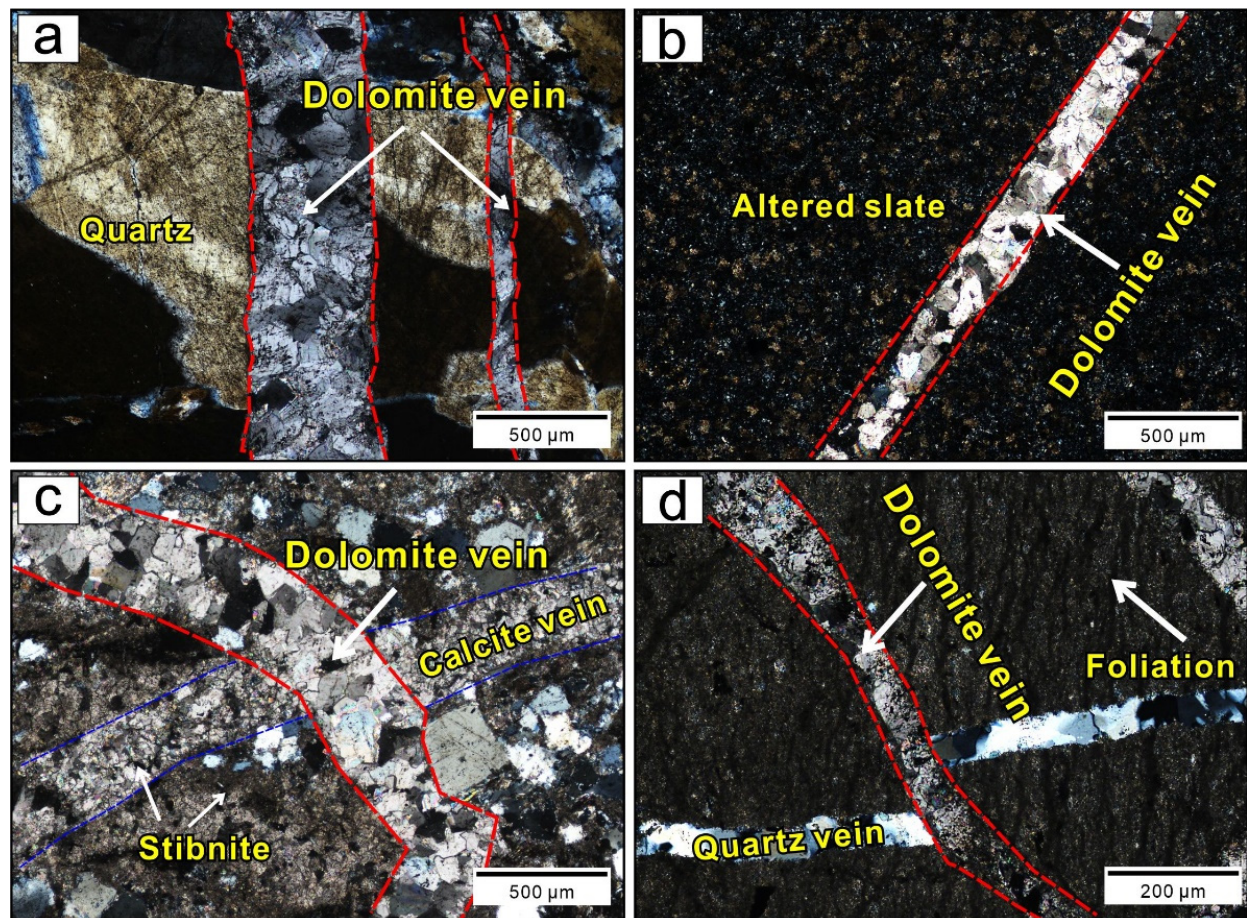


Figure 4. Photomicrograph in samples showing (a,b,d) the dolomite veins cross cut the veinlets correlated with mineralization and wall rock Triassic slate, (c) dolomite vein crosscut calcite vein related to ore.

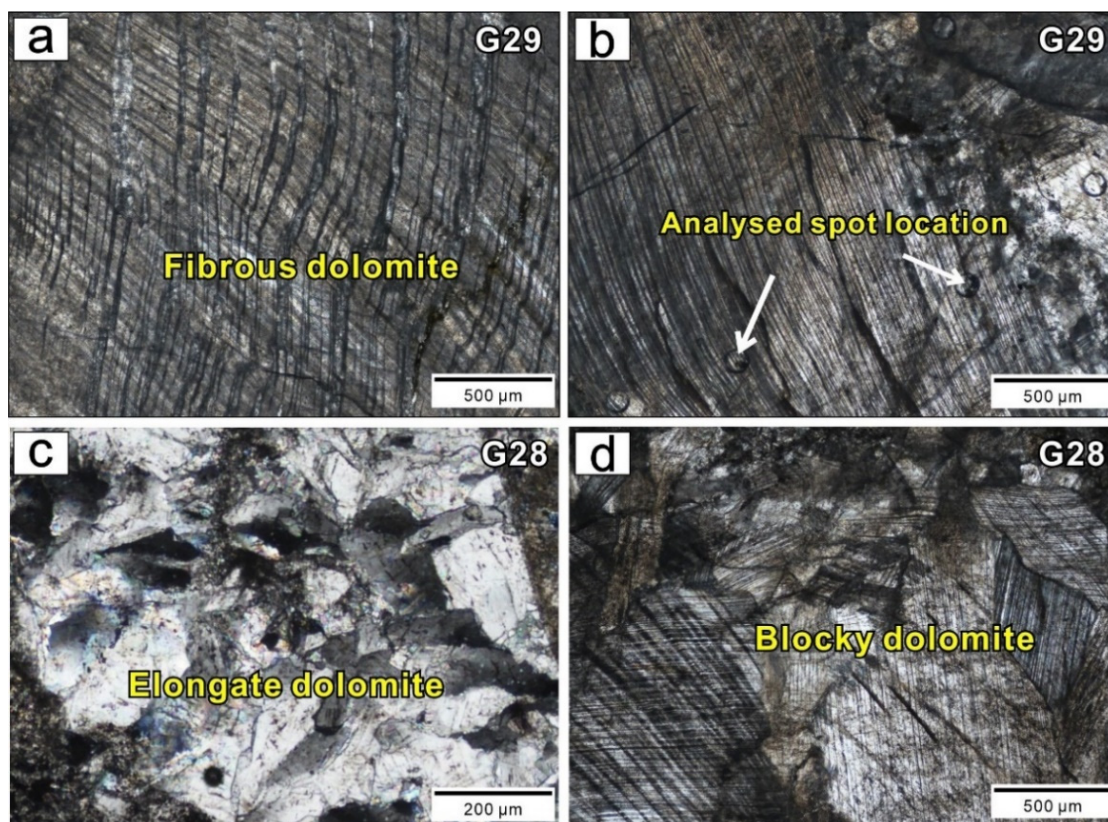


Figure 5. Micrographs of main features of syn-tectonic dolomite crystals. (a) fibrous dolomite crystal from dated samples G29 formed by crack-seal mechanism. (b) locations of U-Pb analyses. (c,d) Elongate and blocky crystals with north-west vein arrays from G28.

3.2. Analytical Methods

All samples were cut into one-inch chips and in thin sections that were polished and examined using optical microscopy and in situ LA-ICP-MS U-Pb dating. Measurement of U-Pb ages from G28 was performed using laser ablation-inductively coupled plasma-mass spectrometry (LA-ICP-MS) in the Key Laboratory of Mineralogy and Metallogeny, Guangzhou Institute of Geochemistry, the Chinese Academy of Sciences. The instrumentation was an Agilent 7900 ICP-MS, coupled to a Resonetics RESolution S-155 ArF Excimer laser source ($\lambda = 193$ nm) (Australian Scientific Instrument, Fyshwick, Australia). Samples were ablated in the conditions with a fluence of 4 J/cm^2 , a beam diameter of $90 \text{ }\mu\text{m}$, and 8 Hz of ablation frequency. U-Pb dating of G29 was carried out with an Element XR sector field inductively coupled plasma-mass spectrometer (Thermo Fisher Scientific, Waltham, MA, USA) coupled to a GeoLasPro 193 nm ArF Excimer laser ablation system ($90 \text{ }\mu\text{m}$ spot size) (CompexPro 102F, Coherent, Shibuya, Tokyo) at the State Key Laboratory of Ore Geochemistry, Institute of Geochemistry Chinese Academy of Sciences. Raw data from both samples were processed to calculate each element concentration offline using the ICPMS Data Cal 11.8 program. We standardized using NIST614 and the WC-1 calcite reference material for normalization [65]. The $^{207}\text{Pb}/^{206}\text{Pb}$ ratios were corrected for mass bias and the $^{206}\text{Pb}/^{238}\text{U}$ ratios for inter-element fraction by using NIST614 and DC. An additional correction has been applied on the $^{206}\text{Pb}/^{238}\text{U}$ to correct for difference in the fractionation due to the carbonate matrix [66]. This resulted in a lower intercept age of 23 WC-1 spot analyses of 254.1 ± 1.5 (MSWD = 1.5). According to the analyzed standard materials, accuracy and repeatability are assumed to be less than 2%. The U-Pb ages were plotted in the Tera-Wasserburg diagram and calculated at 2σ level by ISOPLOT.

4. Results

Field observations illustrate that the fault plane may be locally curved and irregular in detail with 10-cm-width, but generally dips to N and NNW following the regional northwest trend at a steep angle (Figure 2b, oriented $345^\circ/80^\circ$ (strike/dip)). The studied samples consist of dolomite vein precipitated in one fracture related to an extensional set, corresponding to NNW-SSE-trending normal faults. The approximate orientation of main stresses presumably indicates the NW-SE extension for the extensional set (Figure 2). The fracture sets contain fibrous, elongated and blocky dolomite crystals (Figure 5). They have been observed in north-west-trending veins and in parallel veinlets formed by the crack-seal mechanism in normal faults. Fibrous crystals show minimal growth competition (Figure 5a). Elongate dolomite crystals are perpendicular to the fracture walls (Figure 5c). In the faults, blocky crystals are also arranged in stepped sides, which are characterized by the crack-seal mechanism (Figure 5d).

We present U-Pb ages of dolomite from samples G28 and G29 on Tera-Wasserburg inverse concordia diagrams as $^{207}\text{Pb}/^{206}\text{Pb}$ and $^{238}\text{U}/^{206}\text{Pb}$ linear regression isochrons. Thirteen analyses from G28 and nineteen from G29 were carried out. Age data are presented in Figure 5 and listed in Table 1. The obtained U-Pb ages in this study are variable in terms of radiogenic Pb concentrations, the amount of scattering, and the datapoint uncertainties. We have used an objective criterion of age uncertainties less than 20% and an MSWD below 1.0 to screen for robust ages. The U and Pb concentrations in G28 vary ranging from 0.63 to 22.14 ppm (mean = 8.30 ppm, $n = 13$), and 0.93 to 2.75 ppm (mean = 1.93 ppm, $n = 13$), respectively. Such a distribution of U and Pb contents is similar to G29 with the range of 0.02–11.82 ppm (mean = 3.05, ppm, $n = 19$) and 0.37–3.22 ppm (mean = 0.76 ppm, $n = 19$), respectively. A cluster of dates at the radiogenic end of the mixing line from sample G28 is characterized by moderate $^{207}\text{Pb}/^{206}\text{Pb}$ (0.0502–0.8436) and $^{238}\text{U}/^{206}\text{Pb}$ ratios (0.2736–55.7984). Together, all feature an isochron with a lower intercept age of 112 ± 4 Ma (Figure 6), with a mean squared weighted deviation (MSWD) of 0.8. Similarly, sample G29 data show dispersed $^{207}\text{Pb}/^{206}\text{Pb}$ (0.0506–0.8614) and variable $^{238}\text{U}/^{206}\text{Pb}$ ratios (0.2032–55.5003). Regression of all measurements yields a lower intercept age of 115 ± 4 Ma (MSWD = 0.6). All the dated samples show lower initial Pb ratio ($^{207}\text{Pb}/^{206}\text{Pb}$) than would be expected based on the traditional evolution model of the earth (~ 0.83 – 0.86 , [67]).

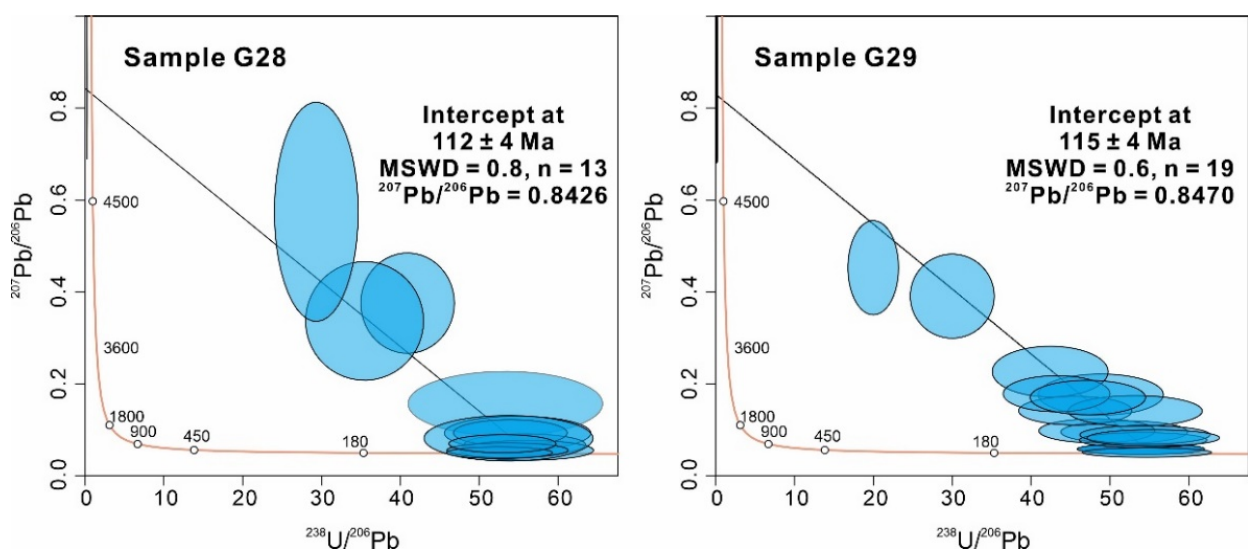


Figure 6. Tera-Wasserburg plot displaying the results of LA-ICP-MS U-Pb spot analyses.

Table 1. LA-ICP-MS dolomite U-Pb dating results of sample G28 and G29.

Sample No.	U		Pb		Isotopic Ratios				Data for Tera-Wasserburg Plot			
	(ppm)	(ppm)	²⁰⁷ Pb/ ²⁰⁶ Pb	²⁰⁷ Pb/ ²³⁵ U	²⁰⁶ Pb/ ²³⁸ U	²³⁸ U/ ²⁰⁶ Pb	²⁰⁷ Pb/ ²⁰⁶ Pb	Ratio	2σ (%)	Ratio	2σ (%)	
Sample G28: 112 ± 4 Ma (MSWD = 0.8, n = 13)												
G28-1	2.39	1.89	0.1567	36.6364	0.4053	31.4640	0.0188	18.9340	53.3126	18.9340	0.1567	36.6364
G28-2	0.84	0.93	0.3754	23.7790	1.2654	20.6608	0.0244	44.2151	40.9096	11.8670	0.3754	23.7790
G28-3	0.96	2.16	0.3367	31.3428	1.3095	26.2138	0.0282	64.4797	35.4539	17.2470	0.3367	31.3428
G28-4	1.27	1.88	0.5742	33.9559	2.6988	30.5942	0.0341	55.2974	29.3367	14.8071	0.5742	33.9559
G28-5	0.63	2.48	0.8436	14.9917	425.1094	10.7071	3.6547	10.7870	0.2736	10.7870	0.8436	14.9917
G28-6	4.73	2.00	0.0926	32.4735	0.2329	29.4827	0.0182	13.8403	54.8600	13.8403	0.0926	32.4735
G28-7	8.91	1.77	0.0677	28.1676	0.1673	25.9286	0.0179	11.2857	55.7984	11.2857	0.0677	28.1676
G28-8	14.46	1.78	0.0933	25.2027	0.2384	22.8373	0.0185	10.9493	53.9414	10.9493	0.0933	25.2027
G28-9	7.65	2.75	0.0554	32.0300	0.1362	29.6699	0.0178	12.3236	56.0498	12.3236	0.0554	32.0300
G28-10	17.11	2.45	0.0815	49.6686	0.2092	46.9798	0.0186	16.3130	53.7124	16.3130	0.0815	49.6686
G28-11	11.79	1.81	0.0555	23.7264	0.1428	20.7784	0.0187	11.7240	53.5892	11.7240	0.0555	23.7264
G28-12	22.14	1.87	0.0502	20.5498	0.1316	17.8650	0.0190	10.4587	52.5565	10.4587	0.0502	20.5498
G28-13	15.07	1.35	0.0697	23.1035	0.1815	20.7303	0.0189	10.5013	52.9373	10.5013	0.0697	23.1035
WC-1	4.51	2.58	0.1297	5.8982	0.7730	6.4404	0.0436	4.4934	22.9198	4.4934	0.1297	5.8982
WC-1	3.39	3.29	0.1011	6.8625	0.6047	7.2190	0.0437	4.3070	22.8680	4.3070	0.1011	6.8625
WC-1	3.25	4.25	0.1140	6.6277	0.6766	7.3305	0.0433	4.5329	23.0891	4.5329	0.1140	6.6277
WC-1	4.91	3.15	0.0993	5.0626	0.5886	6.0451	0.0431	4.2531	23.1931	4.2531	0.0993	5.0626
WC-1	6.14	3.88	0.0883	5.1627	0.5188	6.0586	0.0428	4.1887	23.3636	4.1887	0.0883	5.1627
WC-1	4.10	3.80	0.1192	8.3105	0.7078	8.3710	0.0433	5.6213	23.1037	5.6213	0.1192	8.3105
WC-1	1.98	3.22	0.1219	7.8694	0.7501	8.5609	0.0452	5.0388	22.1408	5.0388	0.1219	7.8694
WC-1	2.49	3.23	0.1165	6.4244	0.6754	7.0079	0.0426	5.1696	23.4833	5.1696	0.1165	6.4244
WC-1	5.03	3.47	0.1286	4.9125	0.7712	6.0391	0.0436	4.3202	22.9499	4.3202	0.1286	4.9125
WC-1	2.96	3.05	0.1370	6.7564	0.8535	7.6606	0.0459	5.7842	21.7912	5.7842	0.1370	6.7564
DC-22	0.30	0.52	0.6298	6.4259	6.9851	160.0553	0.0812	4.9294	11.6281	4.9294	0.6298	6.4259
DC-22	0.46	0.44	0.6150	6.3565	6.6544	160.0062	0.0803	3.6600	11.7605	3.6600	0.6150	6.3565
DC-22	0.50	0.48	0.5910	6.2468	5.4616	160.0969	0.0668	5.1239	14.1228	5.1239	0.5910	6.2468
DC-22	0.44	0.55	0.5485	6.7077	4.5816	160.2109	0.0600	7.0809	15.7324	7.0809	0.5485	6.7077
DC-22	0.74	0.63	0.4989	6.2677	3.5956	160.0178	0.0528	3.8966	17.8780	3.8966	0.4989	6.2677
DC-22	2.21	0.64	0.4794	5.6146	3.3796	160.0327	0.0513	4.1537	18.3996	4.1537	0.4794	5.6146
DC-22	3.75	0.91	0.4276	6.6356	2.7138	160.1018	0.0456	4.4383	20.6872	4.4383	0.4276	6.6356
DC-22	2.03	0.75	0.4302	5.6076	2.6484	160.0163	0.0449	3.6633	21.0442	3.6633	0.4302	5.6076
DC-22	1.36	0.46	0.4306	5.9370	2.4875	160.0035	0.0427	3.7305	22.1072	3.7305	0.4306	5.9370
DC-22	0.43	0.37	0.3763	9.2795	2.0486	160.0945	0.0404	4.9774	23.3644	4.9774	0.3763	9.2795
SRM614	0.81	2.30	0.8683	4.2341	100.5060	9.9902	0.8366	10.0231	1.1953	10.0231	0.8683	4.2341
SRM614	0.80	2.26	0.8699	4.2646	100.0508	9.9873	0.8314	10.1558	1.2027	10.1558	0.8699	4.2646
SRM614	0.81	2.23	0.8731	4.4283	101.3370	10.0288	0.8385	9.9647	1.1926	9.9647	0.8731	4.4283
SRM614	0.83	2.30	0.8729	4.7153	104.0930	9.9765	0.8636	10.0422	1.1579	10.0422	0.8729	4.7153
Sample G29: 115 ± 4 Ma (MSWD = 0.6, n = 19)												
G29-1	11.82	0.43	0.0582	16.7179	0.1401	160.0222	0.0175	12.2717	53.9285	12.2717	0.0582	16.7179
G29-2	0.02	1.00	0.8506	16.2109	540.2476	160.5584	4.6444	18.3680	0.2032	18.3680	0.8506	16.2109
G29-3	2.07	0.45	0.0952	20.9049	0.2371	160.2020	0.0182	12.7026	51.8040	12.7026	0.0952	20.9049
G29-4	1.31	0.43	0.0977	21.8973	0.2599	160.3169	0.0195	12.4539	48.3484	12.4539	0.0977	21.8973
G29-5	0.49	0.37	0.1765	20.7554	0.4538	160.4628	0.0193	13.2886	48.8475	13.2886	0.1765	20.7554
G29-6	7.25	0.41	0.0777	17.0759	0.1855	160.0804	0.0174	12.2361	54.1988	12.2361	0.0777	17.0759
G29-7	0.81	0.39	0.1415	18.0096	0.4029	160.2574	0.0207	12.8902	45.6128	12.8902	0.1415	18.0096
G29-8	22.1	0.42	0.0506	16.6281	0.1196	160.0105	0.0173	12.2506	54.6904	12.2506	0.0506	16.6281
G29-9	0.03	1.36	0.8614	16.1641	872.9977	160.2717	7.3989	15.6118	0.1276	15.6118	0.8614	16.1641
G29-10	1.40	0.45	0.2266	19.9061	0.6984	160.6333	0.0223	14.1691	42.4179	14.1691	0.2266	19.9061
G29-11	0.88	0.41	0.1408	19.4979	0.3467	160.1623	0.0177	13.0635	53.2008	13.0635	0.1408	19.4979
G29-12	2.53	0.44	0.0891	18.4226	0.2122	160.1752	0.0173	12.4064	54.4361	12.4064	0.0891	18.4226
G29-13	1.02	0.42	0.1784	17.9790	0.5247	160.1218	0.0218	12.8153	43.2315	12.8153	0.1784	17.9790
G29-14	0.97	0.41	0.1701	18.0312	0.4603	160.1675	0.0200	12.6787	47.1912	12.6787	0.1701	18.0312
G29-15	2.77	0.39	0.0824	17.6167	0.1930	160.1740	0.0170	12.3722	55.5003	12.3722	0.0824	17.6167

Table 1. Cont.

Sample No.	U		Pb		Isotopic Ratios						Data for Tera-Wasserburg Plot			
	(ppm)	(ppm)	$^{207}\text{Pb}/^{206}\text{Pb}$	$^{207}\text{Pb}/^{206}\text{Pb}$	$^{207}\text{Pb}/^{235}\text{U}$	$^{207}\text{Pb}/^{235}\text{U}$	$^{206}\text{Pb}/^{238}\text{U}$	$^{206}\text{Pb}/^{238}\text{U}$	$^{238}\text{U}/^{206}\text{Pb}$	$^{238}\text{U}/^{206}\text{Pb}$	$^{207}\text{Pb}/^{206}\text{Pb}$	$^{207}\text{Pb}/^{206}\text{Pb}$		
G29-16	1.95	0.54	0.4526	18.5097	3.2820	160.2250	0.0472	13.1588	19.9855	13.1588	0.4526	18.5097		
G29-17	0.54	1.21	0.3907	19.1780	1.7582	160.7674	0.0315	14.5312	29.9960	14.5312	0.3907	19.1780		
G29-18	0.03	1.64	0.8470	16.1228	825.6975	160.4435	7.0660	16.9880	0.1336	16.9880	0.8470	16.1228		
G29-19	0.03	3.22	0.8548	16.0861	2413.3281	160.8984	20.6313	21.0437	0.0458	21.0437	0.8548	16.0861		
WC-1	4.31	0.42	0.1270	8.1554	0.7249	160.0941	0.0416	3.8587	22.6883	3.8587	0.1270	8.1554		
WC-1	3.07	0.42	0.0991	8.3594	0.5567	160.0775	0.0414	3.5575	22.8194	3.5575	0.0991	8.3594		
WC-1	4.13	0.40	0.1001	6.1814	0.5584	160.0369	0.0406	3.6000	23.2675	3.6000	0.1001	6.1814		
WC-1	3.90	0.39	0.0900	6.6186	0.4977	160.0467	0.0402	3.5855	23.4569	3.5855	0.0900	6.6186		
WC-1	6.31	0.57	0.0997	6.6580	0.5527	160.0355	0.0402	3.6454	23.4622	3.6454	0.0997	6.6580		
WC-1	6.37	0.48	0.1046	6.7255	0.5786	160.0256	0.0401	3.2188	23.5308	3.2188	0.1046	6.7255		
WC-1	6.44	0.58	0.0969	7.0842	0.5326	160.0494	0.0400	3.3130	23.5827	3.3130	0.0969	7.0842		
WC-1	6.33	0.41	0.0953	6.9590	0.5244	160.0387	0.0400	3.1891	23.6185	3.1891	0.0953	6.9590		
WC-1	3.95	0.46	0.0991	8.2598	0.5410	160.0345	0.0398	3.3994	23.7210	3.3994	0.0991	8.2598		
WC-1	5.14	0.49	0.1023	6.0575	0.5591	160.0335	0.0398	3.7055	23.7378	3.7055	0.1023	6.0575		
DC-22	0.50	0.50	0.3816	7.4448	1.9338	160.0496	0.0374	4.6791	25.2465	4.6791	0.3816	7.4448		
DC-22	2.99	0.52	0.2488	6.1144	1.0380	160.0278	0.0303	3.3656	31.1637	3.3656	0.2488	6.1144		
DC-22	2.44	0.49	0.2045	6.2530	0.8049	160.0388	0.0287	3.7134	32.8558	3.7134	0.2045	6.2530		
DC-22	0.57	0.41	0.1874	9.6833	0.7146	160.1814	0.0283	5.2267	33.3961	5.2267	0.1874	9.6833		
DC-22	3.40	0.52	0.1894	6.3734	0.7226	160.0310	0.0279	3.4969	33.8873	3.4969	0.1894	6.3734		
DC-22	2.63	0.47	0.2052	6.7612	0.7883	160.0198	0.0272	3.3678	34.6925	3.3678	0.2052	6.7612		
DC-22	2.25	0.46	0.1955	6.3327	0.7295	160.0297	0.0272	3.3547	34.7098	3.3547	0.1955	6.3327		
DC-22	1.84	0.39	0.1613	7.6234	0.6002	160.0757	0.0272	3.5142	34.7254	3.5142	0.1613	7.6234		
DC-22	3.91	0.42	0.1425	6.0823	0.5095	160.0249	0.0260	3.2190	36.3346	3.2190	0.1425	6.0823		
DC-22	0.52	0.43	0.1528	11.0928	0.5319	160.1972	0.0259	4.8258	36.3928	4.8258	0.1528	11.0928		
DC-22	0.50	0.50	0.3816	7.4448	1.9338	160.0496	0.0374	4.6791	25.2465	4.6791	0.3816	7.4448		
SRM614	0.81	2.30	0.8758	4.7325	103.4985	9.9766	0.8572	10.0022	1.1665	10.0022	0.8758	4.7325		
SRM614	0.82	2.31	0.8670	4.9820	105.4558	9.8943	0.8817	10.1101	1.1342	10.1101	0.8670	4.9820		
SRM614	0.83	2.32	0.8729	4.8485	100.6911	9.9891	0.8361	10.0063	1.1961	10.0063	0.8729	4.8485		
SRM614	0.81	2.29	0.8708	3.9581	101.1274	9.9649	0.8381	9.9950	1.1932	9.9950	0.8708	3.9581		

5. Discussion

5.1. Interpretations of Dolomite U-Pb Ages

Carbonate precipitation within fault zones along individual fractures and fault planes is almost ubiquitous and easily recognizable in the field in the forms of slickenfibers, fault gouge, cement and veins [68,69]. Therefore, distinguishing pre-, syn-, and post- kinematic carbonate is key to constraining the timing of fault slip through the carbonate chronometer. The tectonic link could be supported by using careful field observation and petrographic analyses. Veins are intimately related to fracture mechanics, for most veins from by growth of minerals into space are created by fractures [69,70]. Several field occurrences of carbonate precipitation along the fault plane are commonly used to directly infer the timing of fault slip and associated with fracture opening. These include slickenfibres and carbonate filling veins that occurred in extensional jogs, opening-mode fracture with no displacement (single phase), and as multi-phase of sub-parallel contemporaneous carbonates, vuggy crystals growth, and en echelon fractures [71]. Simultaneously, linking mineral precipitation to fault kinematics and associated fracturing processes depends on its origin and morphology. Roberts and Holdsworth (2022) reviewed what examples of carbonate mineralization can more confidently infer the connection than others and how the mechanism can more reliably link to fault kinematics from “crack-seal-slip” [72], “crack-seal” to “crack-fill” types [73]. Ramsay (1980) introduced the term “crack-seal” mechanism, which is appropriate in the context, suggesting the veins, especially those with elongate to fibrous crystals, have been interpreted in terms of this mechanism [74]. Generally, veins exhibit a wide range of internal structures ascribe to various shapes of vein-filling carbonates precipitation and

their growth direction [70,74,75]. As crystals grow side by side in the same direction, the crystals become elongated in the growth direction. If crystals grow into an open space, on growing, nucleation of new crystals suppresses the elongate shape, and more equant grains fill the vein to produce a blocky texture (Figure 5). Fibrous crystals sometimes develop with extreme length/width ratios, and their boundaries are typically smooth. In previous literature, fibrous growth is sometimes attributed to the opening of a vein in small increments, which can only be formed if growth competition is inhibited, while blocky shapes are attributed to growing into an open or fast vein opening [70,76]. In this sense, dolomite showing elongated blocky textures indicate they are syn-kinematic, while blocky textures provide evidence of the precipitation after vein opening or at lower rates than vein opening. Despite this, they are all formed by a crack-seal mechanism, and stepped sides indicate syn-kinematic growth. Such veins, especially crystals precipitation features, indicate the studied dolomite veins are syn-kinematic and occurred synchronously with movement along the fault plane [77–80]. Another key observation linking measured dolomite ages with specific fault motion is that the dolomite precipitation has not been altered or recrystallized, therefore, the explicitly the U-Pb isotopic system has not been reset [81]. The disposition of dolomites in the Gelouang deposit indicates that their growth occurred from both fracture walls to the vein centre and from one vein wall or another vein wall. These crack-seal dolomites fill along the fault direction and record information on growth which is unlikely to have formed during the phases of post-faulting fluid flow and dolomite reprecipitation. In addition, the data points fit within the error of the concordia line and provide a robust estimate of lower intercept ages, suggesting the absence of Pb diffusion. In this case, structural observations suggest the dolomite precipitated synchronous with movement along the fault plane as a consequence of fracture opening. We thus interpret the ages as the precipitation of dolomite veins coeval with the fault formation. The N-W dolomite veins within the fault zone cut Early Triassic slate and orebodies in the Gelouang gold deposit, indicating that the fault formation was later than the host rocks formation and mineralization. The obtained datapoints from dolomite overlap with each other within 2-sigma uncertainties, suggesting that they represent the timing of dolomite formation. The two samples display isochron ages of 112 ± 4 Ma and 115 ± 4 Ma, indicating that the dolomite veins precipitated in the Early Cretaceous.

5.2. Implications for Intracontinental Orogen

In light of the above discussion, the ca. 114 Ma U-Pb ages from the fault date brittle deformations in the Qinling Orogen. These U-Pb ages provide new absolute chronological markers for dating the tectonic events in the Qinling Orogen. The fault is assumed to correlate with the extensional collapse and was interpreted as the consequence of the intracontinental process in the Early Cretaceous. This tectonic evolution history of the Qinling Orogen has been well documented by lines of geological, geophysical, geochemical, and geochronological records on magmatic events from the Early Jurassic to Paleogene [37–39,41,46,52], indicating the diverse units of the Qinling Orogen witnessed complex deformation.

Following the collision in the Triassic, the Qinling Orogen underwent tectonic transition, and the regime changed from compressional deformation to extensional rifting from the Early Jurassic—Early Cretaceous to Late Cretaceous—Paleogene. This intracontinental process is indicated by Mesozoic strata formations with unconformities or angular unconformities near contacts between different tectonic units [38,82]. In the western Qinling Orogen, the Jurassic and Cretaceous strata are also separated by an angular unconformity in places [83]. Similarly, the north margin of the South China Block contains the pre-Cretaceous strata incorporated into the foreland fold-thrust belt, illustrating that the Qinling Orogen evolved into a compressional tectonic setting [37,40]. These southwards fold-thrust deformations were triggered by overthrusts of the South Qinling Terrane [40,42,53,54,82]. After the intensive compression events, the Qinling Orogen evolved into an extensional regime, forming extensive sinistral strike-slip shearing and sinistral-slip-related echelon sedimentary basins along previous faults [42]. Sun et al. (2022) highlighted the decompression and

exhumation phase with mylonites and a ductile shear zone occurring at 119 Ma (Amphibolite Ar-Ar) in the Shagou shear zone [44]. In addition, the 126 to 90 Ma intracontinental deformation phase thermotectonic evolution as inferred from the western and eastern Qinling Orogen is correlated using apatite fission-track data [41,84], which are similar to the deformation and sedimentation investigated in Qinling area [85]. Furthermore, voluminous mafic and felsic magmatism and large-scale Mo-Au-Ag polymetallic mineralization are extensively distributed in the Qinling Orogen [46,86,87]. Their geology and geochemistry suggest an intracontinental extensional setting during the Late Mesozoic [58,88]. For example, a large number of nearly vertical mafic dikes intruded into the western and central part of the Qinling Orogen and showed the ages of ca. 114 Ma (Zircon U-Pb) with a strike roughly parallel to the orogen. Sporadic Late Cretaceous mafic magmatic rocks have been reported in the south margin of the North China Block [89], such as Huanglongpu diabase (129 Ma, Zircon U-Pb), Tianqiaogou diorite (122 Ma, Zircon U-Pb), Funiushan lamprophyre (117 Ma, Zircon U-Pb, [90]), and Niangniangshan granitoids (~123 Ma, Zircon U-Pb, [89]). Ca. 110 Ma felsic dyke intrusion is identified from the Laojunshan region in eastern Qinling Orogen, and shows tectonic regime transformation from compression to extension [88,91].

Taken together, these data mostly record the intracontinental tectonic events and the relative age of deformation and syn-deformational deposition in the eastern part of the Qinling Orogen, while scarce data were available from the western Qinling Orogen. This intracontinental regime is evident from the ages of dolomite veins in the Xiahe-Hezuo district, which crosscut the deformed strata and were emplaced in association with the fault and the intrusions. Synthesizing the above regional works, the dolomite U-Pb ages are close to the period of crustal deformation in the Early Cretaceous, exhibiting an inevitable response to the tectonic evolution occurring within the West Qinling Orogen. The orientations of the analysed normal faults fit with the observed main normal faults related to north-south trend graben/half-graben tectonics in eastern Qinling Orogen. These ages constrain the timing of the brittle deformations of the Qinling Orogen during the Early Cretaceous. This tectonic event appears to be correlated with the intracontinental extensional regime of the Qinling Orogen.

6. Conclusions

- (1) Dolomite from veins along the fault plane was dated with the U-Pb system, yielding ages of 112 ± 4 Ma and 115 ± 4 Ma, which we interpret as reflecting syn-deformational precipitation of the dolomite.
- (2) The new geochronological finding constrains the post-orogenic phase of faulting correlated with intracontinental extensional regime in the Qinling Orogen during the Early Cretaceous. This event exhibits an inevitable response to the tectonic evolution on a regional scale.
- (3) We suggest that U-Pb dating of carbonates like dolomite can constrain the absolute timing of fault motion.

Author Contributions: Conceptualization, G.-P.J.; data curation, Y.-X.G.; funding acquisition, G.-P.J.; investigation, Y.-X.G., G.-P.J., Y.Q., R.-Q.Z., Y.-W.T. and R.Z.; methodology, Y.-X.G., Y.Q., R.-Q.Z., Y.-W.T. and S.-J.Y. project administration, G.-P.J.; software, R.-Q.Z. and Y.-W.T.; writing—original draft preparation, Y.-X.G. and G.-P.J.; writing—review and editing, Y.Q., R.-Q.Z. and Y.-W.T. All authors have read and agreed to the published version of the manuscript.

Funding: This research was funded by the National Nature Science Foundation of China (42072087), the 111 Project (BP071902), the Beijing Nova Program (Z201100006820097) and the National Key Research Program (2019YFA0708603).

Data Availability Statement: All the data is presented in the paper.

Acknowledgments: The authors are very grateful for logistic assistance from the management of Zaozigou Gold Company.

Conflicts of Interest: The authors declare no conflict of interest.

References

1. Haines, S.H.; van der Pluijm, B.A. Dating the detachment fault system of the Ruby Mountains, Nevada: Significance for the kinematics of low-angle normal faults. *Tectonics* **2010**, *29*. [[CrossRef](#)]
2. Viola, G.; Scheiber, T.; Fredin, O.; Zwingmann, H.; Margreth, A.; Knies, J. Deconvoluting complex structural histories archived in brittle fault zones. *Nat. Commun.* **2016**, *7*, 13448. [[CrossRef](#)] [[PubMed](#)]
3. Zwingmann, H.; Mancktelow, N. Timing of Alpine fault gouges. *Earth Planet. Sci. Lett.* **2004**, *223*, 415–425. [[CrossRef](#)]
4. Li, Q.; Parrish, R.; Horstwood, M.; McArthur, J. U–Pb dating of cements in Mesozoic ammonites. *Chem. Geol.* **2014**, *376*, 76–83. [[CrossRef](#)]
5. Roberts, N.M.; Walker, R.J. U–Pb geochronology of calcite-mineralized faults: Absolute timing of rift-related fault events on the northeast Atlantic margin. *Geology* **2016**, *44*, 531–534. [[CrossRef](#)]
6. Rasbury, E.T.; Present, T.M.; Northrup, P.; Tappero, R.V.; Lanzirotti, A.; Cole, J.M.; Wooton, K.M.; Hatton, K. Tools for uranium characterization in carbonate samples: Case studies of natural U–Pb geochronology reference materials. *Geochronology* **2021**, *3*, 103–122. [[CrossRef](#)]
7. Tang, Y.; Gao, J.; Lan, T.; Cui, K.; Han, J.; Zhang, X.; Chen, Y.; Chen, Y. In situ low-U garnet U–Pb dating by LA-SF-ICP-MS and its application in constraining the origin of Anji skarn system combined with Ar–Ar dating and Pb isotopes. *Ore Geol. Rev.* **2021**, *130*, 103970. [[CrossRef](#)]
8. Zhang, R.; Lehmann, B.; Seltnann, R.; Sun, W.; Li, C. Cassiterite U–Pb geochronology constrains magmatic-hydrothermal evolution in complex evolved granite systems: The classic Erzgebirge tin province (Saxony and Bohemia). *Geology* **2017**, *45*, 1095–1098. [[CrossRef](#)]
9. Roberts, N.; Drost, K.; Horstwood, M.; Condon, D.; Drake, H.; Milodowski, A.; Mclean, N.; Smye, A.; Haslam, R.; Hodson, K. LA-ICP-MS U–Pb carbonate geochronology: Strategies, progress, and application to fracture-fill calcite. *Geochronol. Discuss.* **2020**. [[CrossRef](#)]
10. Ring, U.; Gerdes, A. Kinematics of the Alpenrhein-Bodensee graben system in the Central Alps: Oligocene/Miocene transtension due to formation of the Western Alps arc. *Tectonics* **2016**, *35*, 1367–1391. [[CrossRef](#)]
11. Hansman, R.J.; Albert, R.; Gerdes, A.; Ring, U. Absolute ages of multiple generations of brittle structures by U–Pb dating of calcite. *Geology* **2018**, *46*, 207–210. [[CrossRef](#)]
12. Nuriel, P.; Weinberger, R.; Kylander-Clark, A.; Hacker, B.; Craddock, J. The onset of the Dead Sea transform based on calcite age-strain analyses. *Geology* **2017**, *45*, 587–590. [[CrossRef](#)]
13. Nuriel, P.; Wotzlaw, J.-F.; Ovtcharova, M.; Vaks, A.; Stremtan, C.; Šala, M.; Roberts, N.M.; Kylander-Clark, A.R. The use of ASH-15 flowstone as a matrix-matched reference material for laser-ablation U–Pb geochronology of calcite. *Geochronology* **2021**, *3*, 35–47. [[CrossRef](#)]
14. Mottram, C.M.; Kellett, D.A.; Barresi, T.; Zwingmann, H.; Friend, M.; Todd, A.; Percival, J. Syncing fault rock clocks: Direct comparison of U–Pb carbonate and K–Ar illite fault dating methods. *Geology* **2020**, *48*, 1179–1183. [[CrossRef](#)]
15. Coogan, L.A.; Parrish, R.R.; Roberts, N.M. Early hydrothermal carbon uptake by the upper oceanic crust: Insight from in situ U–Pb dating. *Geology* **2016**, *44*, 147–150. [[CrossRef](#)]
16. Godeau, N.; Deschamps, P.; Guihou, A.; Leonide, P.; Tendil, A.; Gerdes, A.; Hamelin, B.; Girard, J.-P. U–Pb dating of calcite cement and diagenetic history in microporous carbonate reservoirs: Case of the Urgonian Limestone, France. *Geology* **2018**, *46*, 247–250. [[CrossRef](#)]
17. Manganot, X.; Gasparrini, M.; Gerdes, A.; Bonifacie, M.; Rouchon, V. An emerging thermochronometer for carbonate-bearing rocks: $\Delta 47$ /(U–Pb). *Geology* **2018**, *46*, 1067–1070. [[CrossRef](#)]
18. MacDonald, J.; Faithfull, J.; Roberts, N.; Davies, A.; Holdsworth, C.; Newton, M.; Williamson, S.; Boyce, A.; John, C. Clumped-isotope palaeothermometry and LA-ICP-MS U–Pb dating of lava-pile hydrothermal calcite veins. *Contrib. Mineral. Petrol.* **2019**, *174*, 63. [[CrossRef](#)]
19. Shen, A.; Hu, A.; Cheng, T.; Liang, F.; Pan, W.; Feng, Y.; Zhao, J. Laser ablation in situ U–Pb dating and its application to diagenesis-porosity evolution of carbonate reservoirs. *Pet. Explor. Dev.* **2019**, *46*, 1127–1140. [[CrossRef](#)]
20. Yang, P.; Wu, G.; Nuriel, P.; Nguyen, A.D.; Chen, Y.; Yang, S.; Feng, Y.-x.; Ren, Z.; Zhao, J.-x. In situ LA-ICPMS UPb dating and geochemical characterization of fault-zone calcite in the central Tarim Basin, northwest China: Implications for fluid circulation and fault reactivation. *Chem. Geol.* **2021**, *568*, 120125. [[CrossRef](#)]
21. Deng, J.; Yang, L.-Q.; Groves, D.I.; Zhang, L.; Qiu, K.-F.; Wang, Q.-F. An integrated mineral system model for the gold deposits of the giant Jiaodong province, eastern China. *Earth Sci. Rev.* **2020**, *208*, 103274. [[CrossRef](#)]
22. Hu, Y.; Cai, C.; Liu, D.; Pederson, C.L.; Jiang, L.; Shen, A.; Immenhauser, A. Formation, diagenesis and palaeoenvironmental significance of upper Ediacaran fibrous dolomite cements. *Sedimentology* **2020**, *67*, 1161–1187. [[CrossRef](#)]
23. Mueller, M.; Igbokwe, O.A.; Walter, B.; Pederson, C.L.; Riechelmann, S.; Richter, D.K.; Albert, R.; Gerdes, A.; Buhl, D.; Neuser, R.D. Testing the preservation potential of early diagenetic dolomites as geochemical archives. *Sedimentology* **2020**, *67*, 849–881. [[CrossRef](#)]
24. Roberts, N.M.; Lee, J.K.; Holdsworth, R.E.; Jeans, C.; Farrant, A.R.; Haslam, R. Near-surface Palaeocene fluid flow, mineralisation and faulting at Flamborough Head, UK: New field observations and U–Pb calcite dating constraints. *Solid Earth* **2020**, *11*, 1931–1945. [[CrossRef](#)]

25. Salih, N.; Mansurbeg, H.; Kolo, K.; Gerdes, A.; Pr at, A. In situ U-Pb dating of hydrothermal diagenesis in tectonically controlled fracturing in the Upper Cretaceous Bekhme Formation, Kurdistan Region-Iraq. *Int. Geol. Rev.* **2020**, *62*, 2261–2279. [[CrossRef](#)]
26. Luo, K.; Zhou, J.-X.; Feng, Y.-X.; Uysal, I.T.; Nguyen, A.; Zhao, J.-X.; Zhang, J. In situ U-Pb dating of calcite from the South China antimony metallogenic belt. *Science* **2020**, *23*, 101575. [[CrossRef](#)]
27. Jin, X.-Y.; Zhao, J.-X.; Feng, Y.-X.; Hofstra, A.H.; Deng, X.-D.; Zhao, X.-F.; Li, J.-W. Calcite U-Pb dating unravels the age and hydrothermal history of the giant Shuiyindong Carlin-type gold deposit in the golden triangle, South China. *Econ. Geol.* **2021**, *116*, 1253–1265. [[CrossRef](#)]
28. Deng, J.; Qiu, K.-F.; Wang, Q.-F.; Goldfarb, R.; Yang, L.-Q.; Zi, J.-W.; Geng, J.-Z.; Ma, Y. In situ dating of hydrothermal monazite and implications for the geodynamic controls on ore formation in the Jiaodong gold province, eastern China. *Econ. Geol.* **2020**, *115*, 671–685. [[CrossRef](#)]
29. Qiu, K.; Yu, H.; Wu, M.; Geng, J.; Ge, X.; Gou, Z.; Taylor, R.D. Discrete Zr and REE mineralization of the Baerzhe rare-metal deposit, China. *Am. Mineral. J. Earth Planet. Mater.* **2019**, *104*, 1487–1502. [[CrossRef](#)]
30. Yu, H.-C.; Qiu, K.-F.; Hetherington, C.J.; Chew, D.; Huang, Y.-Q.; He, D.-Y.; Geng, J.-Z.; Xian, H.-Y. Apatite as an alternative petrochronometer to trace the evolution of magmatic systems containing metamict zircon. *Contrib. Mineral. Petrol.* **2021**, *176*, 68. [[CrossRef](#)]
31. Wu, M.; Samon, I.; Qiu, K.; Zhang, D. Multi-stage metasomatic Zr mineralization in the world-class Baerzhe Rare earth element-Nb-Zr-Be deposit. *Am. Miner.* **2022**, *in press*. [[CrossRef](#)]
32. Wu, M.; Samson, I.; Qiu, K.; Zhang, D. Concentration mechanisms of REE-Nb-Zr-Be mineralization in the Baerzhe deposit, NE China: Insights from textural and chemical features of amphibole and rare-metal minerals. *Econ. Geol.* **2021**, *116*, 651–679. [[CrossRef](#)]
33. Qiu, K.-F.; Yu, H.-C.; Hetherington, C.; Huang, Y.-Q.; Yang, T.; Deng, J. Tourmaline composition and boron isotope signature as a tracer of magmatic-hydrothermal processes. *Am. Mineral. J. Earth Planet. Mater.* **2021**, *106*, 1033–1044. [[CrossRef](#)]
34. Long, Z.-Y.; Qiu, K.-F.; Santosh, M.; Yu, H.-C.; Jiang, X.-Y.; Zou, L.-Q.; Tang, D.-W. Fingerprinting the metal source and cycling of the world’s largest antimony deposit in Xikuangshan, China. *GSA Bull.* **2022**. [[CrossRef](#)]
35. Wang, Y.; Qiu, K.F.; M uller, A.; Hou, Z.L.; Zhu, Z.H.; Yu, H.C. Machine Learning Prediction of Quartz Forming-Environments. *J. Geophys. Res. Solid Earth* **2021**, *126*, e2021JB021925. [[CrossRef](#)]
36. Dong, Y.; Zhang, G.; Neubauer, F.; Liu, X.; Genser, J.; Hauzenberger, C. Tectonic evolution of the Qinling orogen, China: Review and synthesis. *J. Asian Earth Sci.* **2011**, *41*, 213–237. [[CrossRef](#)]
37. Dong, Y.; Santosh, M. Tectonic architecture and multiple orogeny of the Qinling Orogenic Belt, Central China. *Gondwana Res.* **2016**, *29*, 1–40. [[CrossRef](#)]
38. Zhang, G.; Zhang, B.; Yuan, X.C.; Xiao, Q. *Qinling Orogenic Belt and Continental Dynamics*; Science Press: Beijing, China, 2001. (In Chinese with English Abstract)
39. Liu, J.; Zhang, P.; Lease, R.O.; Zheng, D.; Wan, J.; Wang, W.; Zhang, H. Eocene onset and late Miocene acceleration of Cenozoic intracontinental extension in the North Qinling range–Weihe graben: Insights from apatite fission track thermochronology. *Tectonophysics* **2013**, *584*, 281–296. [[CrossRef](#)]
40. Dong, Y.; Yang, Z.; Liu, X.; Sun, S.; Li, W.; Cheng, B.; Zhang, F.; Zhang, X.; He, D.; Zhang, G. Mesozoic intracontinental orogeny in the Qinling Mountains, central China. *Gondwana Res.* **2016**, *30*, 144–158. [[CrossRef](#)]
41. Hu, S.; Raza, A.; Min, K.; Kohn, B.P.; Reiners, P.W.; Ketchum, R.A.; Wang, J.; Gleadow, A.J. Late Mesozoic and Cenozoic thermotectonic evolution along a transect from the north China craton through the Qinling orogen into the Yangtze craton, central China. *Tectonics* **2006**, *25*. [[CrossRef](#)]
42. Li, J.; Zhang, Y.; Dong, S.; Shi, W. Structural and geochronological constraints on the Mesozoic tectonic evolution of the North Dabashan zone, South Qinling, central China. *J. Asian Earth Sci.* **2013**, *64*, 99–114. [[CrossRef](#)]
43. Heberer, B.; Anzenbacher, T.; Neubauer, F.; Genser, J.; Dong, Y.; Dunkl, I. Polyphase exhumation in the western Qinling Mountains, China: Rapid Early Cretaceous cooling along a lithospheric-scale tear fault and pulsed Cenozoic uplift. *Tectonophysics* **2014**, *617*, 31–43. [[CrossRef](#)] [[PubMed](#)]
44. Sun, S.; Dong, Y.; Cheng, C.; He, D.; Zhou, B.; Liu, X. Mesozoic intracontinental ductile shearing along the Paleozoic Shangdan suture in the Qinling Orogen: Constraints from deformation fabrics and geochronology. *GSA Bull.* **2022**. [[CrossRef](#)]
45. Qiu, K.F.; Deng, J. Petrogenesis of granitoids in the Dewulu skarn copper deposit: Implications for the evolution of the Paleotethys ocean and mineralization in Western Qinling, China. *Ore Geol. Rev.* **2017**, *90*, 1078–1098. [[CrossRef](#)]
46. Qiu, K.-F.; Yu, H.-C.; Deng, J.; McIntire, D.; Gou, Z.-Y.; Geng, J.-Z.; Chang, Z.-S.; Zhu, R.; Li, K.-N.; Goldfarb, R. The giant Zaozigou Au-Sb deposit in West Qinling, China: Magmatic-or metamorphic-hydrothermal origin? *Mineral. Depos.* **2020**, *55*, 345–362. [[CrossRef](#)]
47. Yu, H.-C.; Qiu, K.-F.; Pirajno, F.; Zhang, P.-C.; Dong, W.-Q. Revisiting Phanerozoic evolution of the Qinling Orogen (East Tethys) with perspectives of detrital zircon. *Gondwana Res.* **2022**, *103*, 426–444. [[CrossRef](#)]
48. Yu, H.-C.; Qiu, K.-F.; Nassif, M.-T.; Geng, J.-Z.; Sai, S.-X.; Duo, D.-W.; Huang, Y.-Q.; Wang, J. Early orogenic gold mineralization event in the West Qinling related to closure of the Paleo-Tethys Ocean—Constraints from the Ludousou gold deposit, central. *Ore Geol. Rev.* **2020**, *117*, 103217. [[CrossRef](#)]

49. Yang, L.-Q.; Deng, J.; Dilek, Y.; Qiu, K.-F.; Ji, X.-Z.; Li, N.; Taylor, R.D.; Yu, J.-Y. Structure, geochronology, and petrogenesis of the Late Triassic Puziba granitoid dikes in the Mianlue suture zone, Qinling orogen, China. *GSA Bull.* **2015**, *127*, 1831–1854. [[CrossRef](#)]
50. Qiu, K.-F.; Yu, H.-C.; Gou, Z.-Y.; Liang, Z.-L.; Zhang, J.-L.; Zhu, R. Nature and origin of Triassic igneous activity in the Western Qinling Orogen: The Wenquan composite pluton example. *Int. Geol. Rev.* **2018**, *60*, 242–266. [[CrossRef](#)]
51. Qiu, K.-F.; Taylor, R.D.; Song, Y.-H.; Yu, H.-C.; Song, K.-R.; Li, N. Geologic and geochemical insights into the formation of the Taiyangshan porphyry copper–molybdenum deposit, Western Qinling Orogenic Belt, China. *Gondwana Res.* **2016**, *35*, 40–58. [[CrossRef](#)]
52. Dong, Y.; Zhang, G.; Hauzenberger, C.; Neubauer, F.; Yang, Z.; Liu, X. Palaeozoic tectonics and evolutionary history of the Qinling orogen: Evidence from geochemistry and geochronology of ophiolite and related volcanic rocks. *Lithos* **2011**, *122*, 39–56. [[CrossRef](#)]
53. Hu, J.; Chen, H.; Qu, H.; Wu, G.; Yang, J.; Zhang, Z. Mesozoic deformations of the Dabashan in the southern Qinling orogen, central China. *J. Asian Earth Sci.* **2012**, *47*, 171–184. [[CrossRef](#)]
54. Shi, W.; Zhang, Y.; Dong, S.; Hu, J.; Wiesinger, M.; Ratschbacher, L.; Jonckheere, R.; Li, J.; Tian, M.; Chen, H. Intra-continental Dabashan orocline, southwestern Qinling, central China. *J. Asian Earth Sci.* **2012**, *46*, 20–38. [[CrossRef](#)]
55. Yu, H.C.; Qiu, K.F.; Deng, J.; Zhu, R.; Mathieu, L.; Sai, S.X.; Sha, W.J. Exhuming and preserving epizonal orogenic Au-Sb deposits in rapidly uplifting orogenic settings. *Tectonics* **2022**, *41*, e2021TC007165. [[CrossRef](#)]
56. Sui, J.; Li, J.; Jin, X.; Vasconcelos, P.; Zhu, R. 40Ar/39Ar and U-Pb constraints on the age of the Zaozigou gold deposit, Xiahe-Hezuo district, West Qinling orogen, China: Relation to early Triassic reduced intrusions emplaced during slab rollback. *Ore Geol. Rev.* **2018**, *101*, 885–899. [[CrossRef](#)]
57. Luo, B.; Zhang, H.; Xu, W.; Yang, H.; Zhao, J.; Guo, L.; Zhang, L.; Tao, L.; Pan, F.; Gao, Z. The magmatic plumbing system for Mesozoic high-Mg andesites, garnet-bearing dacites and porphyries, rhyolites and leucogranites from West Qinling, central China. *J. Petrol.* **2018**, *59*, 447–482. [[CrossRef](#)]
58. Jin, X.; Li, J.; Sui, J.; Wen, G.; Zhang, J. Geochronological and Geochemical Constraints on the Genesis and Tectonic Setting of Dewulu Intrusive Complex in Xiahe-Hezuo District of Western Qinling. *J. Earth Sci. Environ.* **2013**, *35*, 20–38. (In Chinese with English Abstract)
59. Hou, G. Mechanism for three types of mafic dyke swarms. *Geosci. Front.* **2012**, *3*, 217–223. [[CrossRef](#)]
60. Craddock, W.H.; Kirby, E.; Dewen, Z.; Jianhui, L. Tectonic setting of Cretaceous basins on the NE Tibetan Plateau: Insights from the Jungong basin. *Basin Res.* **2012**, *24*, 51–69. [[CrossRef](#)]
61. Mao, J.; Xie, G.; Zhang, Z.; Li, X.; Wang, Y.; Zhang, C.; Li, Y. Mesozoic large-scale metallogenic pulses in North China and corresponding geodynamic settings. *Acta Petrol. Sin.* **2005**, *1*, 169–188. (In Chinese with English Abstract)
62. Yang, L.-Q.; Deng, J.; Qiu, K.-F.; Ji, X.-Z.; Santosh, M.; Song, K.-R.; Song, Y.-H.; Geng, J.-Z.; Zhang, C.; Hua, B. Magma mixing and crust–mantle interaction in the Triassic monzogranites of Bikou Terrane, central China: Constraints from petrology, geochemistry, and zircon U–Pb–Hf isotopic systematics. *J. Asian Earth Sci.* **2015**, *98*, 320–341. [[CrossRef](#)]
63. Deng, J.; Wang, Q. Gold mineralization in China: Metallogenic provinces, deposit types and tectonic framework. *Gondwana Res.* **2016**, *36*, 219–274. [[CrossRef](#)]
64. Huang, Y.; Qiu, K.; Yu, H.; Jin, D.; He, D.; Xiao, C.; Wang, Y. Petrogenesis of ore-hosting porphyry in the Geluang gold deposit, West Qinling and its geological implications. *Acta Petrol. Sin.* **2020**, *36*, 1567–1585. (In Chinese with English Abstract)
65. Roberts, N.M.; Rasbury, E.T.; Parrish, R.R.; Smith, C.J.; Horstwood, M.S.; Condon, D.J. A calcite reference material for LA-ICP-MS U-Pb geochronology. *Geochem. Geophys. Geosyst.* **2017**, *18*, 2807–2814. [[CrossRef](#)]
66. Guillong, M.; Wotzlaw, J.-F.; Looser, N.; Laurent, O. Evaluating the reliability of U–Pb laser ablation inductively coupled plasma mass spectrometry (LA-ICP-MS) carbonate geochronology: Matrix issues and a potential calcite validation reference material. *Geochronology* **2020**, *2*, 155–167. [[CrossRef](#)]
67. Stacey, J.t.; Kramers, J. Approximation of terrestrial lead isotope evolution by a two-stage model. *Earth Planet. Sci. Lett.* **1975**, *26*, 207–221. [[CrossRef](#)]
68. Lee, Y.-J.; Morse, J.W. Calcite precipitation in synthetic veins: Implications for the time and fluid volume necessary for vein filling. *Chem. Geol.* **1999**, *156*, 151–170. [[CrossRef](#)]
69. Bons, P.D.; Elburg, M.A.; Gomez-Rivas, E. A review of the formation of tectonic veins and their microstructures. *J. Struct. Geol.* **2012**, *43*, 33–62. [[CrossRef](#)]
70. Bons, P.D. The formation of veins and their microstructures. *J. Virtual Explor.* **2000**, *2*, 12. [[CrossRef](#)]
71. Fossen, H. *Structural Geology*; Cambridge University Press: Cambridge, UK, 2016.
72. Petit, J.-P.; Wibberley, C.A.; Ruiz, G. ‘Crack–seal’, slip: A new fault valve mechanism? *J. Struct. Geol.* **1999**, *21*, 1199–1207. [[CrossRef](#)]
73. Roberts, N.M.; Holdsworth, R.E. Timescales of faulting through calcite geochronology: A review. *J. Struct. Geol.* **2022**, *158*, 104578. [[CrossRef](#)]
74. Ramsay, J.G. The crack–seal mechanism of rock deformation. *Nature* **1980**, *284*, 135–139. [[CrossRef](#)]
75. Bons, P.D.; Montenari, M. The formation of antitaxial calcite veins with well-developed fibres, Oppaminda Creek, South Australia. *J. Struct. Geol.* **2005**, *27*, 231–248. [[CrossRef](#)]

76. Bons, A.-J.; Bons, P.D. The development of oblique preferred orientations in zeolite films and membranes. *Microporous Mesoporous Mater.* **2003**, *62*, 9–16. [[CrossRef](#)]
77. Caputo, R.; Hancock, P.L. Crack-jump mechanism of microvein formation and its implications for stress cyclicity during extension fracturing. *J. Geodyn.* **1998**, *27*, 45–60. [[CrossRef](#)]
78. Holland, M.; Urai, J.L. Evolution of anastomosing crack–seal vein networks in limestones: Insight from an exhumed high-pressure cell, Jabal Shams, Oman Mountains. *J. Struct. Geol.* **2010**, *32*, 1279–1290. [[CrossRef](#)]
79. Williams, R.T.; Mozley, P.S.; Sharp, W.D.; Goodwin, L.B. U-Th Dating of Syntectonic Calcite Veins Reveals the Dynamic Nature of Fracture Cementation and Healing in Faults. *Geophys. Res. Lett.* **2019**, *46*, 12900–12908. [[CrossRef](#)]
80. Oren, O.; Nuriel, P.; Kylander-Clark, A.R.; Haviv, I. Evolution and Propagation of an Active Plate Boundary: U-Pb Ages of Fault-Related Calcite From the Dead Sea Transform. *Tectonics* **2020**, *39*, e2019TC005888. [[CrossRef](#)]
81. Roberts, N.; Drost, K.; Horstwood, M.; Condon, D.; Chew, D.; Drake, H.; Milodowski, A.; McLean, N.; Smye, A.; Walker, R.; et al. Laser ablation inductively coupled plasma mass spectrometry (LA-ICP-MS) U–Pb carbonate geochronology: Strategies, progress, and limitations. *Geochronology* **2020**, *2*, 33–61. [[CrossRef](#)]
82. Dong, Y.; Zha, X.; Fu, M.; Zhang, Q.; Yang, Z.; Zhang, Y. Characteristics of the Dabashan fold-thrust nappe structure at the southern margin of the Qinling, China. *Geol. Bull. China* **2008**, *27*, 1493–1508. (In Chinese with English Abstract)
83. Guo, J.; Han, W.; Li, X. The cenozoic tectonic evolution of the West Qinling: Constraints on the uplift and deformation of the Qinghai-Tibet Plateau. *Earth Sci. Front.* **2009**, *16*, 215–225. [[CrossRef](#)]
84. Ratschbacher, L.; Franz, L.; Enkelmann, E.; Jonckheere, R.; Pörschke, A.; Hacker, B.R.; Dong, S.; Zhang, Y. The Sino-Korean-Yangtze suture, the Huwan detachment, and the Paleozoic-Tertiary exhumation of (ultra) high-pressure rocks along the Tongbai-Xinxian-Dabie Mountains. *Spec. Pap.-Geol. Soc. Am.* **2006**, *403*, 45.
85. Shen, C.; Hu, D.; Shao, C.; Mei, L. Thermochronology quantifying exhumation history of the Wudang Complex in the South Qinling Orogenic Belt, central China. *Geol. Mag.* **2018**, *155*, 893–906. [[CrossRef](#)]
86. Goldfarb, R.; Qiu, K.-F.; Deng, J.; Chen, Y.; Yang, L. Orogenic gold deposits of China. *SEG Spec. Publ.* **2019**, *22*, 263–324.
87. Qiu, K.-F.; Goldfarb, R.J.; Deng, J.; Yu, H.-C.; Gou, Z.-Y.; Ding, Z.-J.; Wang, Z.-K.; Li, D.-P. Gold deposits of the Jiaodong Peninsula, eastern China. *SEG Spec. Publ.* **2020**, *23*, 753–773.
88. Zhang, F.; Cawood, P.A.; Dong, Y.; Wang, Y. Petrogenesis and tectonic implications of Early Cretaceous andesitic–dacitic rocks, western Qinling (Central China): Geochronological and geochemical constraints. *Geosci. Front.* **2019**, *10*, 1507–1520. [[CrossRef](#)]
89. Gao, X.; Zhao, T. Late Mesozoic magmatism and tectonic evolution in the Southern margin of the North China Craton. *Sci. China Earth Sci.* **2017**, *60*, 1959–1975. [[CrossRef](#)]
90. Gao, X.; Zhao, T.; Gao, J.; Xue, L.; Yuan, Z. LA-ICP-MS zircon U-Pb ages, Hf isotopic composition and geochemistry of adakitic granites in the Xiaoqinling region, the south margin of the North China block. *Geochimica* **2012**, *41*, 303–325.
91. Yang, F.; Xue, F.; Santosh, M.; Wang, G.; Kim, S.W.; Shen, Z.; Jia, W.; Zhang, X. Late Mesozoic magmatism in the East Qinling Orogen, China and its tectonic implications. *Geosci. Front.* **2019**, *10*, 1803–1821. [[CrossRef](#)]